





Formation and Eruption of Sigmoidal Structure from a Weak Field Region of NOAA 11942

N. Vasantharaju¹ , P. Vemareddy² , B. Ravindra², and V. H. Doddamani¹
¹Department of Physics, Bangalore University, Bengaluru-560 056, India; vrajuap@gmail.com
²Indian Institute of Astrophysics, Koramangala, Bengaluru-560 034, India

Received 2018 November 27; revised 2019 February 13; accepted 2019 February 19; published 2019 April 5

Abstract

Using observations from the *Solar Dynamics Observatory*, we studied an interesting example of a sigmoid formation and eruption from small-scale flux-canceling regions of active region (AR) 11942. Through an analysis of Helioseismic and Magnetic Imager and Atmospheric Imaging Assembly observations we infer that initially the AR is compact and bipolar in nature, evolved to a sheared configuration consisting of inverse J-shaped loops hosting a filament channel over a couple of days. By tracking the photospheric magnetic features, shearing and converging motions are observed to play a prime role in the development of S-shaped loops and further flux cancellation leads to tether-cutting reconnection of J loops. This phase is cotemporal with the filament rise motion, followed by sigmoid eruption at 21:32 UT on January 6. The flux rope rises in phases of slow ($v_{\text{avg}} = 26 \text{ km s}^{-1}$) and fast ($a_{\text{avg}} = 55 \text{ m s}^{-2}$) rise motion categorizing the coronal mass ejection (CME) as slow with an associated weak C1.0 class X-ray flare. The flare ribbon separation velocity peaks at around the peak time of the flare at which the maximum reconnection rate (2.14 V cm^{-1}) occurs. Furthermore, the extreme ultraviolet light curves of 131, 171 Å have delayed peaks of 130 minutes compared to 94 Å and are explained by differential emission measure. Our analysis suggests that the energy release is preceded by a much longer time duration, manifesting the onset of the filament rise and an eventual eruption driven by converging and canceling flux in the photosphere. Unlike strong eruption events, the observed slow CME and weak flare are indications of slow runaway tether-cutting reconnection in which most of the sheared arcade is relaxed during the extended phase after the eruption.

Key words: Sun: activity – Sun: coronal mass ejections (CMEs) – Sun: flares – Sun: general – Sun: magnetic fields

Supporting material: animation

1. Introduction

Understanding solar coronal mass ejection (CME) has been a major research objective for the past two decades due to its ability to affect the space weather tremendously. Hence, many studies have explored forecasting such eruptions by determining the necessary eruptive conditions based on their source regions (Falconer 2001; Falconer et al. 2003; Leka & Barnes 2003a, 2003b; Schrijver 2007; Vemareddy & Mishra 2015; Vasantharaju et al. 2018). Also, the appearance of S-shaped structure, or inverse S-shaped structure, or simply “sigmoid” in the coronal active region (AR) is considered to be a progenitor of CMEs (Rust & Kumar 1996; Chen 2011). Generally, the sheared and twisted field lines in sigmoidal structure possess large amounts of magnetic free energy that is released during CME. S-shaped sigmoids are mostly observed in the southern hemisphere and inverse S-shaped sigmoids are observed in the northern hemisphere (Rust & Kumar 1996; Pevtsov et al. 2001). This is consistent with the predominantly negative current helicity observed in the northern hemisphere and positive current helicity observed in the southern hemisphere (Seehafer 1990; Pevtsov et al. 1995). ARs possessing sigmoids are significantly more likely to be eruptive than non-sigmoid ARs (Canfield et al. 1999). The sigmoid is now regarded as an important signature in space weather forecasts (Rust et al. 2005; Vemareddy & Mishra 2015).

Past statistical studies confirm that the majority of CMEs have a clear magnetic flux rope (MFR) structure (Vourlidis et al. 2013). Since the coronal magnetic field cannot be measured directly, the flux rope model can only seek indirect evidence from observations. Rust & Kumar (1996) proposed

that sigmoidal structure in an AR can be explained with the flux rope model. Later, several studies explored the flux rope model with numerical experiments that reproduced many of the observational properties of the sigmoid (Gibson et al. 2006).

The major questions about these flux ropes are how do they form and how do they produce eruptions. Sigmoid eruptions are interpreted using two kinds of observational models based on two different viewpoints of the same structure as sheared arcade and flux rope. The first kind of model assumes that the sigmoid is composed of a sheared and twisted core field in the AR and the internal/external runaway tether-cutting reconnection is responsible for the sigmoid-to-arcade transformation and eruption (Antiochos et al. 1999; Moore et al. 2001). The second kind of model argues that the evolution of a sigmoidal AR with a flare and CME is explained by a twisted MFR in the form of a filament structure that emerges and equilibrates with the overlying coronal magnetic field structure (Gibson et al. 2006). van Ballegoijen & Martens (1989) proposed a scenario of flux rope formation from a sheared arcade in which flux cancellation occurs due to slow shearing and converging regions about the polarity inversion line (PIL).

From the magnetohydrodynamic (MHD) point of view, the flux rope is in equilibrium under the balance of magnetic pressure in the flux rope and the magnetic tension of the overlying magnetic field. If the twist number increases to some critical value, then kink instability occurs (Hood & Priest 1979; Török et al. 2004). If the decay index of the background field, in which the MFR is embedded, is larger than some critical value, torus instability can occur (Kliem & Török 2006; Aulanier et al. 2010). However, in general both ideal MHD

instability and magnetic reconnection mechanisms are responsible for the release of magnetic energy by triggering the flux rope eruption successfully (Forbes 2000). These models are similar to the catastrophe model in which the flux rope loses equilibrium after reaching a critical height, forming a current sheet beneath it, connecting the post-CME loops to the CME ejecta (Lin et al. 2005; Bemporad et al. 2006), as predicted by both the classical CSHKP flare model (Carmichael 1964; Sturrock 1966; Hirayama 1974; Kopp & Pneuman 1976) and other CME models (e.g., Lin & Forbes 2000; Chen et al. 2007).

Generally, the catastrophe model efficiently explains the observed CME-flare-associated eruptions rather than flareless CME events. Quite recently, Song et al. (2013) studied the energy release mechanisms in a sample of 13 flareless CME events, which are associated with prominence eruptions that originated from relatively weak-field quiet-Sun regions. They found that the ideal MHD flux rope instability plays a major role in the magnetic energy release process, while the magnetic reconnection plays the minor role. This manuscript presents a comprehensive study of the formation, initiation, and eruption of a sigmoid from a weak-field AR. We try to understand the weak eruption by asking the following three questions. (1) Under what conditions did the eruption occurs? (2) What conditions made it weak (in terms of CME speed, energy, and associated flare class)? (3) How are the observed consequences different from strong eruption events?. In Section 2 we describe the observational data. The results are presented in Section 3. In Section 4 we provide our conclusions and a summary.

2. Observational Data

The Atmospheric Imaging Assembly (AIA; Lemen et al. 2012) on board the *Solar Dynamics Observatory* (SDO; Pesnell et al. 2012) produces full-disk extreme ultraviolet (EUV) images in 10 wavelength bands at a high cadence of 12 s and pixel size of $0''.6$. For the present study, we used the images obtained at 94 Å (Fe XVIII; $T \sim 6.4$ MK), 131 Å (Fe XXI; $T \sim 10$ MK), 171 Å (Fe IX; $T \sim 0.6$ MK), 193 Å (Fe XII; $T \sim 1.6$ MK and Fe XXIV; $T \sim 20$ MK), and 304 Å (He II; $T \sim 0.05$ MK) wavelengths. To increase the contrast and signal-to-noise ratio, we added five consecutive images to give a cadence of 1 minute. The corresponding photospheric magnetic field observations are obtained from the Helioseismic and Magnetic Imager (HMI; Scherrer et al. 2012) on board SDO. Both line-of-sight (LOS) and vector magnetic field measurements obtained at a cadence of 12 minutes are used in this study. The vector data set is `hmi.sharp_cea_720s` series, which provides automatically selected cutouts of ARs (space weather HMI AR patches; SHARPs—see Bobra et al. 2014) in the form of Lambert cylindrical equal-area (CEA) projection. Using the cutout image processing aide provided by the JSOC Stanford website, the cutouts of LOS full-disk magnetogram data were used and then these cutouts were corrected for the area foreshortening that occurs away from the central meridian. The CME was observed in white light by the Large Angle and Spectrometric Coronagraph (LASCO; Brueckner et al. 1995) on board *SOHO*, which consists of two optical systems, C2 (2.2–6.0 R_{\odot}) and C3 (4–32 R_{\odot}).

3. Analysis and Results

AR NOAA 11942 first appeared as a compact region on 2014 January 1 in the eastern limb of the northern hemisphere.

It was of Mount Wilson class- $\alpha\gamma$, gradually evolving to class- $\beta\gamma$ while moving across the disk toward the west limb, and finally revert to class- $\alpha\gamma$ before it decays on 2014 January 10. During the disk passage, AR 11942 possessed an inverse S sigmoidal structure in EUV wavebands during its decay phase on 2014 January 6–7. The fragmentation and dispersion of both the north and south polarity regions led to the formation of a sigmoid and it supported the filament at the initial stages. In due course the filament got separated from the sigmoid and started to rise upward, leading to a CME associated with a small X-ray flare. The inverse S-shaped structure indicates the region has left-handed chirality or negative helicity (Pevtsov 2002). Motivated by these observations, we studied the formation of sigmoidal structure, and the driving and triggering mechanisms of the eruption from sigmoidal AR.

3.1. Slow Evolution and Build-up of Sigmoidal Loop Structure

To present the typical evolution of AR 11942, we used characteristic snapshots of AIA 171 Å on different days, overlaid with corresponding LOS magnetogram contours, shown in the bottom panels of Figure 1. The magnetograms are shown in the top panels. The AR consists of leading negative and following positive polarity mimicking a bipolar configuration. We noticed from these panels that the positive and negative polarity regions were in a compact and less dispersed phase on 2014 January 3, and the coronal loop structure in AIA 171 Å images indicates a simple potential-field configuration (first column of Figure 1). Furthermore, on January 4 (second column of Figure 1), the positive polarity regions start to diffuse toward the southern direction, whereas negative polarity elements start to undergo further fragmentation and dispersion toward the west. This process as a whole manifests converging and shearing motion of magnetic patches in the interfering region of the leading negative and following positive polarities (see also Figure 2). While this process continues until January 5 (third column of Figure 1), the AR loops become increasingly sheared, with an inverse S-shaped morphology due to the combination of the two inverse J-shaped loops joining at the middle. During this process, we also noticed the emergence of positive magnetic flux near the negative polarity region toward the west, which further complicates the magnetic topology of the AR. We can see the difference in simple potential configuration on January 3 and that of inverse S-shaped sigmoidal loop structure on January 5.

3.2. Shearing and Converging Motions

To study the converging and shearing flux motions, we derived a horizontal velocity field with a differential affine velocity estimator (Schuck 2006) technique. We use HMI LOS magnetogram maps at a 12 minute cadence. In order to highlight large-scale and long-term flow patterns, the velocity maps are averaged over 4 hr. These flow velocities are shown in Figure 2. Vectors indicate the direction of flux motion within a region of polarity outlined by a contour at ± 100 G. We normalized the magnitude of velocity vectors to 0.6 km s^{-1} such that the features that move at far less velocity will be clearly visible. From Figure 2(a), the velocity field in the negative polarity shows a flow pattern toward the east and that in positive polarity indicates a flow pattern toward the west. These flow patterns around the PIL of the region manifest

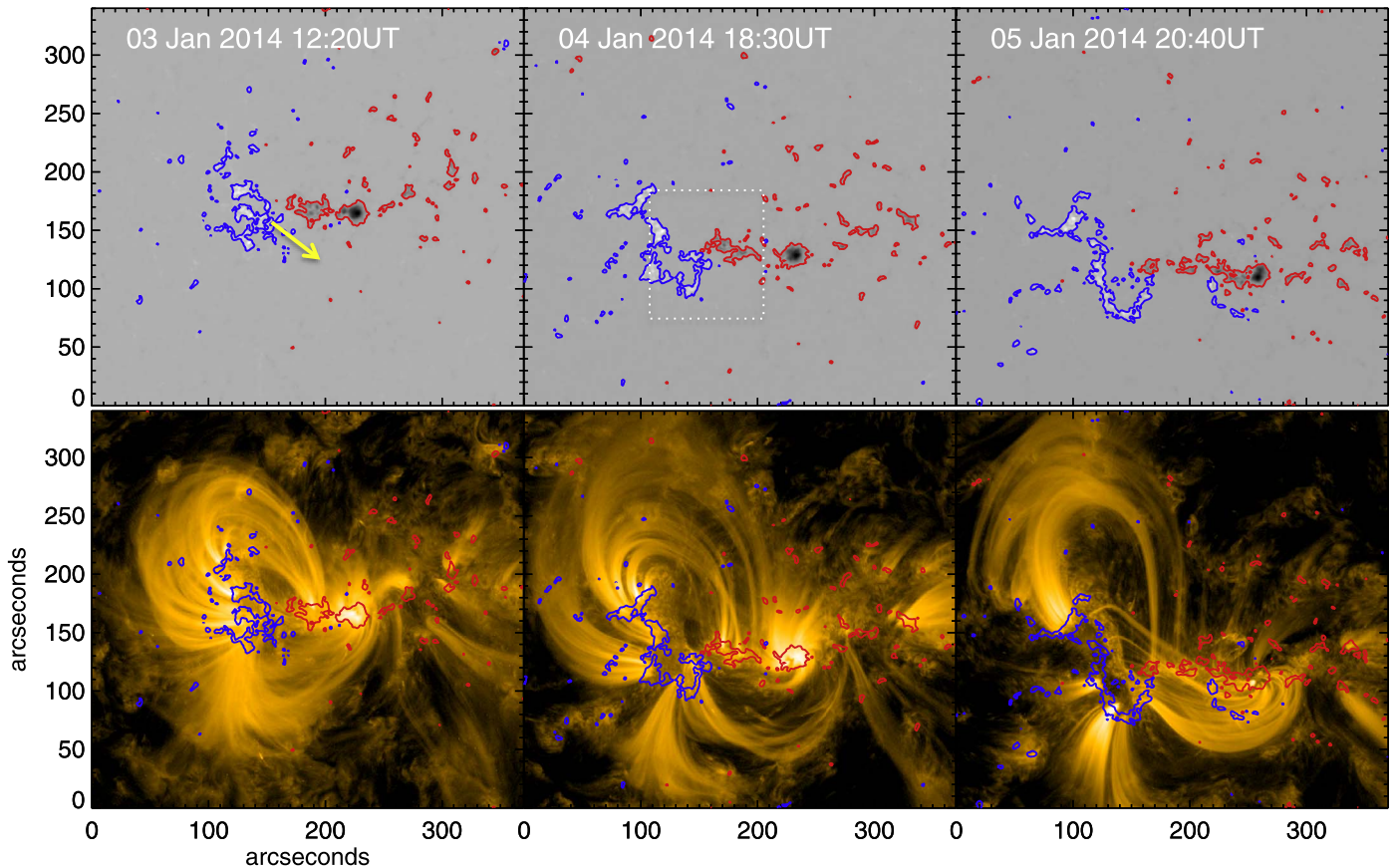


Figure 1. Observations of AR 11942 evolution over days. Top row: LOS magnetic field observations with contours at ± 100 G. The yellow arrow indicates the direction of shear motion of positive polarity and the dotted rectangular box in 04/18:30 UT panel contains the interacting region of positive and negative polarities to further examine the flux motions. Bottom row: AIA 171 Å observations showing the build-up of inverse S-shaped sheared arcade from potential-like loop structure on January 3. Bz-contours at ± 100 G are overlaid to identify the polarity of the loop foot points.

shearing motion. This motion is known to effectively transform the initial potential configuration to a sheared arcade, which then undergoes reconnection at the converging region to form sigmoidal configurations (Amari et al. 2003). In the subsequent instances, the velocity patterns in both the polarities indicate that flows are converging toward each other (within the orange oval). These motions about the PIL cause the flux cancellation process. Chae et al. (2004) reported that submerging opposite polarities are the sites of canceling magnetic features. In addition to the sigmoid formation due to the slow shear and converging motions, a filament channel is observed in AIA 304 Å images from January 5, which implies a flux rope topology in which dipped field lines support the filament material.

3.3. Filament Initiation and the Onset of Main-phase Reconnection

In Figure 3(a), the filament is seen to be supported by sigmoidal structure. This filament channel exhibits some dynamical activity early on January 6 that is cotemporal with the net flux decrease from the flux cancellation process. During this period, the filament channel appears to rise higher in height, especially the north lobe segment. These observations imply that continued shearing and converging motion of the fluxes lead to the onset of a filament rise motion by the tether-cutting reconnection from around 05:35 UT. In Figure 3(b), the rising filament is captured in an AIA 304 Å image at 17:10 UT.

After 21:00 UT the filament becomes invisible to the AIA 304 Å passband, as it had risen to a higher altitude, and eventually erupts at 21:32 UT.

The morphological transformation in the sheared arcade during the filament eruption (i.e., from 20:00 UT to 01:00 UT on January 6) is demonstrated with AIA EUV observations in Figure 4. The first and second row images are from two hotter passbands, AIA 94 Å (6.4 MK) and AIA 131 Å (10 MK), respectively, whereas the third row images are from a relatively cooler passband, AIA 171 Å (0.6 MK). The bundle of two sheared inverse J-shaped loops is evident in the second column images of Figure 4 and also traced in the AIA 131 Å image (middle row) as a yellow dashed lines. These two loops eventually get reconnected to form the long inverse S-shaped loop as depicted in the subsequent third and fourth column images of Figure 4. Observations of continuous flux cancellation by converging and shearing motions suggests the tether-cutting reconnection model (Moore & Labonte 1980), where the inverse J-shaped field lines come closer and reconnect to form long inverse S-shaped loops. Due to this tether-cutting reconnection, we expect that the sigmoidal field lines will be heated to higher temperatures ($>2-20$ MK) and the resultant enhanced emission is captured in hotter AIA 94 Å, AIA 131 Å, and AIA 193 Å passbands, whereas the cooler AIA 171 Å passband could not detect the emission enhancement from the heated plasma from reconnection. This scenario is highlighted by white arrows in the second column. From the AIA movies of 94 Å and 131 Å, we observed the initial

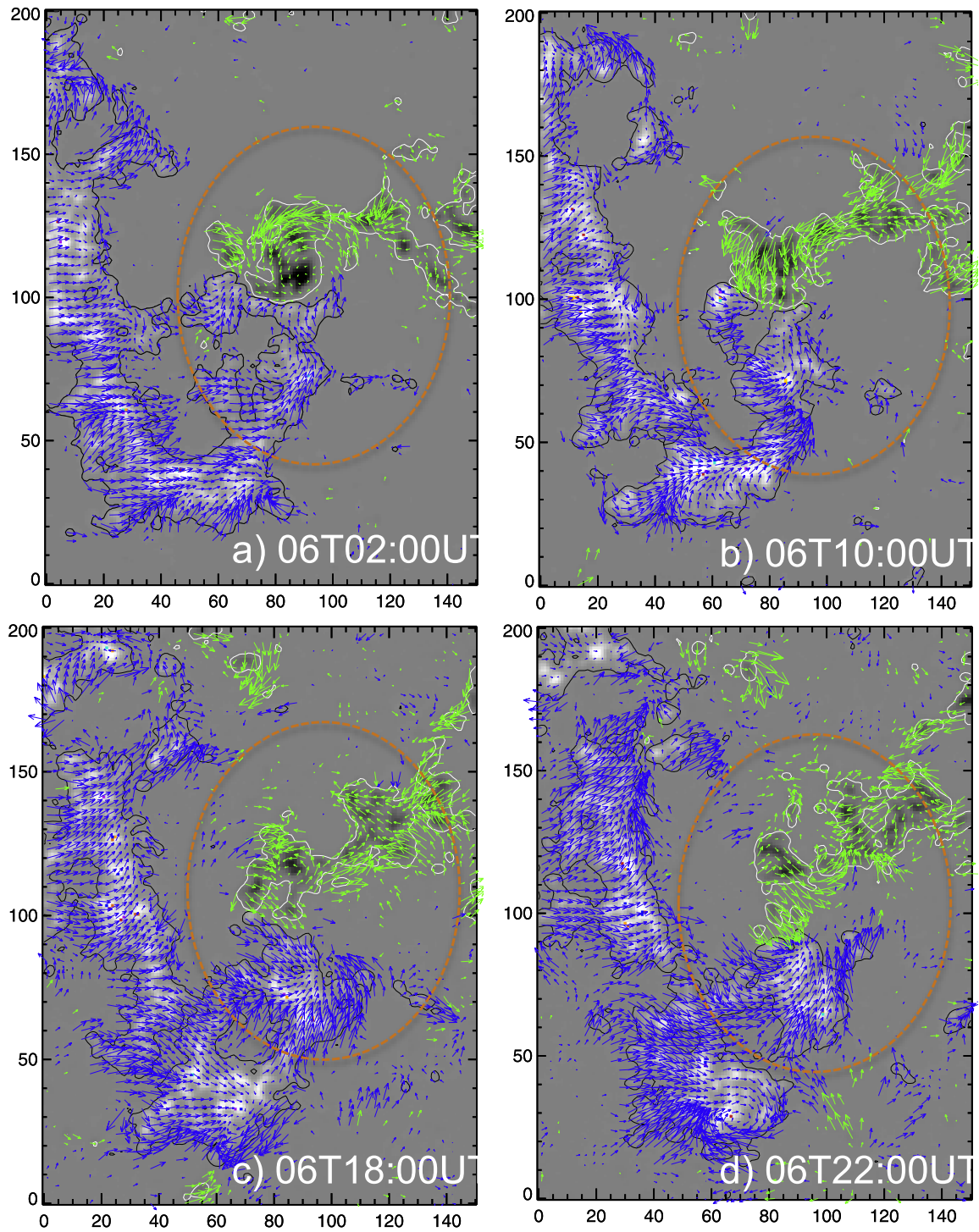


Figure 2. Horizontal velocity of flux motions in the interacting region of positive and negative polarities (rectangular box in Figure 1). The derived velocities from HMI LOS B_z (12 minute cadence) are averaged over 4 hr to enhance the large-scale motion of the fluxes. The arrows indicate the direction of motion and their length is proportional to the magnitude of a maximum of 0.6 km s^{-1} . Both the positive and negative polarities in each panel move toward each other and interact through converging motion in a region enclosed by an orange oval. In all panels, axis units are in pixels of $0''.5$.

enhanced brightness due to reconnection at 21:32 UT on January 6, which is presumed to be the time of the onset of the main-phase reconnection between two inverse J-shaped loops. The addition of axial flux strengthens the flux-rope and is seen as an expanding CME on the northwest side, which is not directly visible in EUV images but is clear in the running difference images of AIA 171 Å. Furthermore, the repetitive reconnection continues in the sheared arcade and the emission

of the resultant heated plasma is suggested to be responsible for the brightening of the observed transient sigmoidal structure.

3.3.1. Flare Ribbon Velocity and Reconnection Rate

We observed the flare ribbons and their separation from 21:40 UT on January 6 to about 01:00 UT on 7 January in AIA 304 Å passband images. To track the flare ribbon motion, we

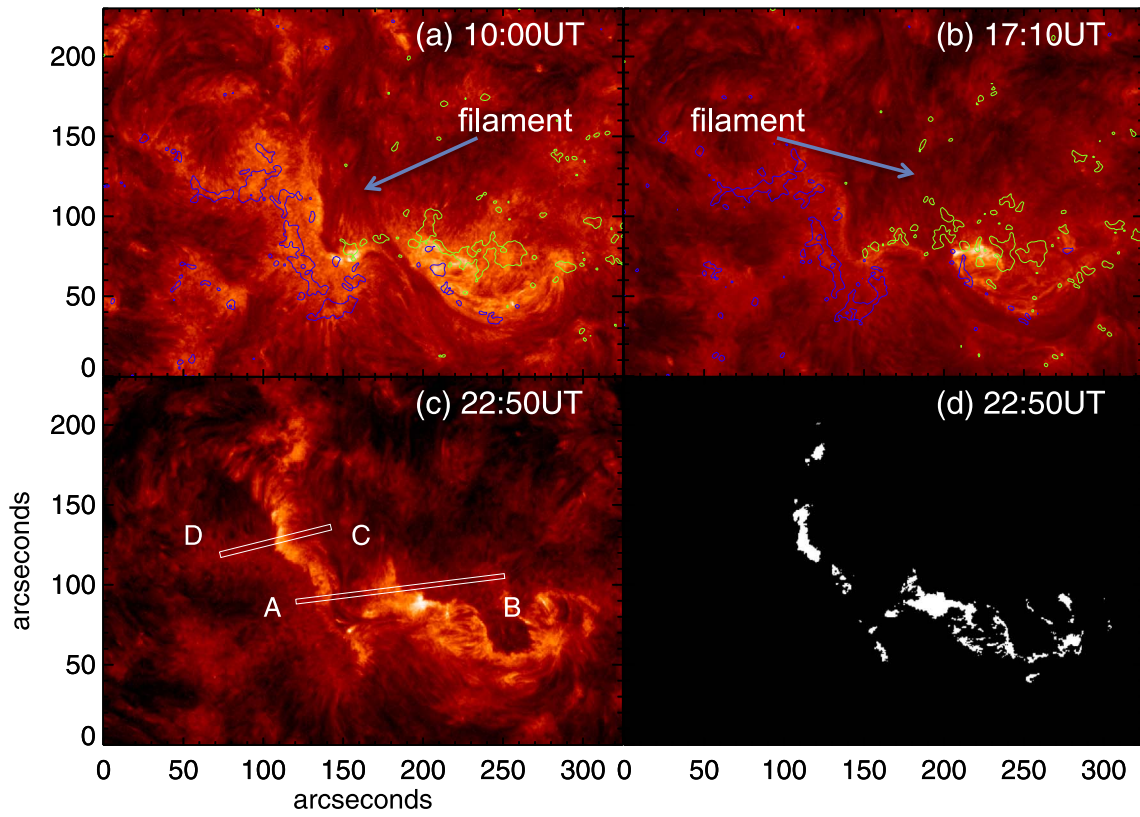


Figure 3. AIA 304 Å observations on 2014 January 6 showing a filament rise motion during the flux cancellation phase. (a) At 10:00 UT the filament was seen as an integral part of the sigmoidal structure. (b) At 17:10 UT the filament appeared to be rising. Contours of LOS magnetic field observations at ± 100 G are overlaid in panels (a) and (b). (c) At 22:50 UT the flare ribbons were observed after the filament eruption. Slices AB and CD were placed to track the ribbon motions. (d) Flare ribbon mask generated from panel (c), used to compute the mean magnetic field strength swept by flare ribbons at 22:50 UT.

used the AIA 304 Å images at a cadence of 2 minutes and determined the ribbon separation velocities using slices at different directions along ribbon motion as shown in Figure 3(c). The stack-up of one such slice (AB) with time is shown in the top panel of Figure 5. To smooth out fluctuations due to measurement uncertainties, spline smoothing was applied to the distance data points, which are identified as being tracked from the front edge of the flare ribbon. The spline fit to the flare ribbon distance profile is marked with blue “+” symbols. The required temporal evolution of the apparent ribbon velocity was determined as the time derivative of the spline-smoothed distance profiles and is shown as an inset (green) in the top panel of Figure 5.

Forbes & Priest (1984) and Forbes & Lin (2000) showed that the local reconnection rate, i.e., the rate at which magnetic field lines are carried into the reconnection site, is given by the coronal electric field E at the reconnection site. They derived a simple relation between the local reconnection rate and the apparent flare ribbon separation speed v . It is given by $E = B_n v$, where B_n is the normal component of the magnetic field’s underlying flare ribbon location. To determine the photospheric magnetic field strength, first we generated the flare ribbon mask by determining the intensity threshold ($\geq 10^{2.5}$ DN s $^{-1}$ pixel $^{-1}$) of the AIA 304 Å image. The masks are generated at a cadence of 2 minutes for every AIA 304 Å image. One such example mask is shown in panel 3(d). Later, the masks are multiplied with a near simultaneous coregistered LOS magnetograms to get the underlying magnetic field swept by a flare ribbon front. To reduce the uncertainty, we excluded the

magnetogram pixels with values less than 20 G in the computation of the absolute mean of the photospheric magnetic field. The temporal profiles of mean magnetic field strength and local reconnection rate are plotted in the bottom panel of Figure 5. The velocity of the flare ribbon (one moving toward the west) and the local reconnection rate reach their maximum values of 11.52 km s $^{-1}$ and 2.14 V cm $^{-1}$, respectively, at 21:47 UT (± 1 minute) and are cotemporal with the flare peak time. Our results are comparable with the maximum reconnection rates obtained for C-class eruptive flares in Hinterreiter et al. (2018) and are less than the maximum reconnection rates obtained for strong eruptive flares (Miklenic et al. 2007; Hinterreiter et al. 2018).

3.4. Post-eruption Evolution and the CME

3.4.1. Light Curves

The evolution of the GOES soft X-ray (SXR) flux in 1–8 Å and the light curves of AR 11942 obtained from AIA images of different wavelengths are shown in the top and bottom panels of Figure 6, respectively. The GOES SXR background is already above the C-class due to the X-ray flux from other ARs and there was a sudden small flux enhancement corresponding to the EUV flux from AR 11942 at 21:32 UT (black vertical dotted line). Unlike many eruptive flares, this SXR enhancement of the C1.0 flare lasts for an hour and is regarded as weak, compared to the long EUV activity. A time delay between the peak emissions of different EUV wavelengths is noticeable in the bottom panel of Figure 6. All these light curves were normalized to their maximum intensity and

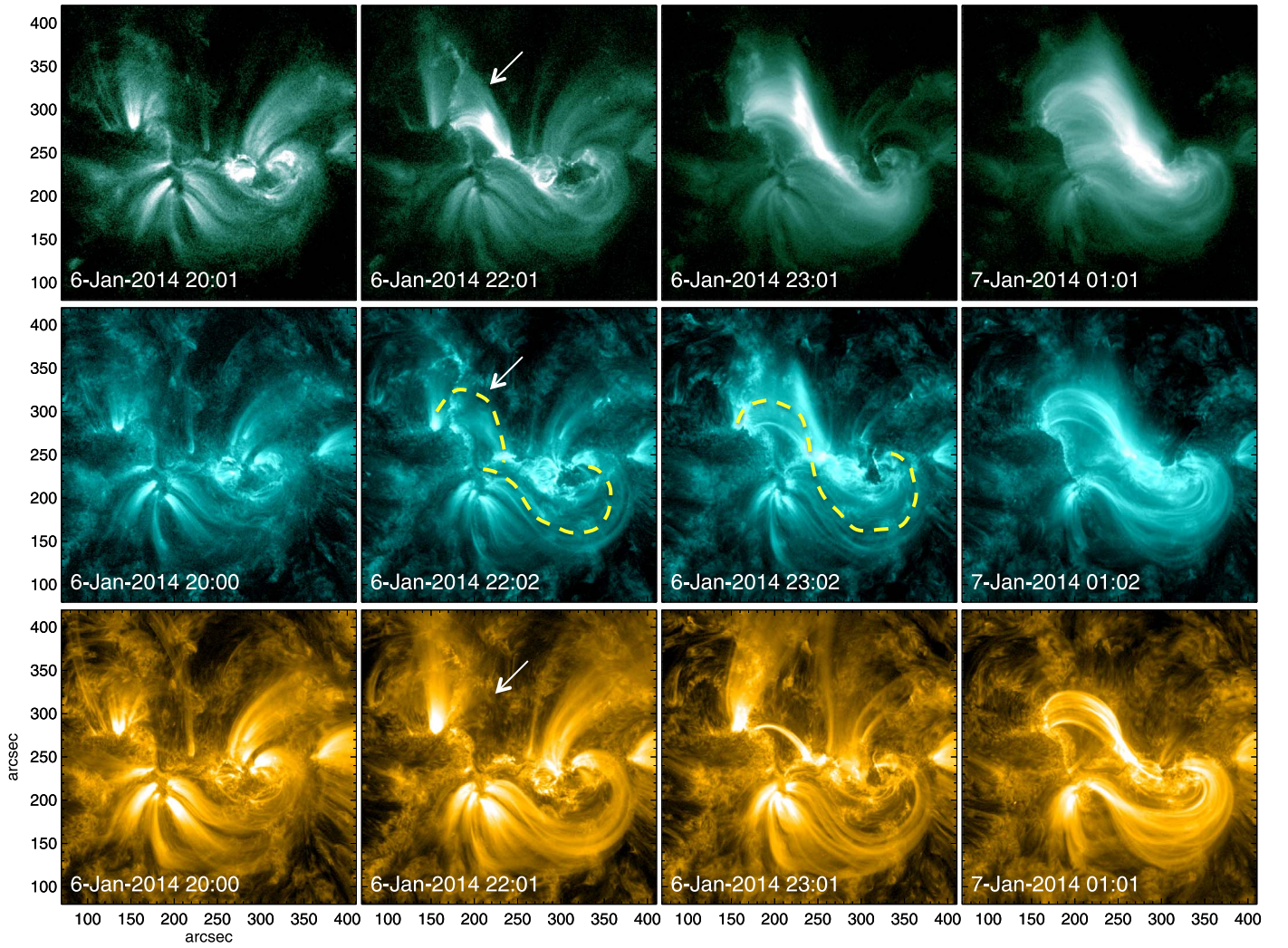


Figure 4. Observations showing the onset of eruption through reconnection of inverse J-shaped loops. First row: images in the AIA 94 Å waveband. Second row: images in AIA 131 Å waveband. Third row: AIA 171 Å waveband. During reconnection, the hot loop system develops; this is shown with white arrows in the second column. The yellow dashed lines trace the inverse J-shaped loops and the S-shaped loop in the second and third AIA 131 Å images (second row), respectively.

were vertically shifted by some amount to avoid overlapping of these curves.

The time profile of AIA 94 Å starts rising at 21:32 UT and reaches peak emission at 00:44 UT on January 7, followed by a slow decay phase. The emission from hot coronal inverse S-shaped loops was clearly captured in AIA 94 Å and AIA 131 Å. The 131 Å filter covers Fe VIII ($\text{Log } T \approx 5.6$), Fe XX ($\text{Log } T \approx 7.1$), and Fe XXIII ($\text{Log } T \approx 7.2$), which are sensitive to low temperatures at 0.6 MK and high temperatures at 10 MK as well. The 131 Å has peak emission from the AR at 2:54 UT on January 7 and is delayed by 130 minutes compared to AIA 94 Å. The additional heating provided by the slow magnetic reconnection in the gradual phase creates the delayed peak emission in AIA 131 (Liu et al. 2015). Light curve of AIA 304 shows an impulsive rise and reaches quickly to its peak at January 6, 22:40 UT even before the AIA 94 light curve. This shows that the chromosphere and transition region immediately responded to heating to at least 1 MK (Chamberlin et al. 2012) and its wider peak is accounted for by different cooling timescales of the heated coronal loops. A dip in the AIA 171 profile during main-phase reconnection is mainly due to the hot reconnection loops, which are opaque to the cooler passband of AIA 171 (Dai et al. 2018). Later, these loops slowly start to

appear in AIA 171 and warm coronal emission peaks at 2:52 UT on January 7, which is mainly due to the long cooling process of the late-phase loops, as proposed in Liu et al. (2013). Note that the AIA 171 and AIA 131 peak emissions (both the AIA 131 and AIA 171 passbands are sensitive to cooler temperatures of ≈ 0.6 MK) got delayed by about 130 minutes compared to AIA 94 Å. Also, such time delays in the peak emissions of the light curves of strong eruptions (which occurred in the ARs of, for example, Vemareddy & Zhang 2014) are quite smaller (≈ 10 minutes). Though studies like Liu et al. (2015) and Dai et al. (2018) also observed the large time delays between peak emissions in EUV light curves of ARs during confined flare events, we need more comparative studies between strong and weak eruptive ARs to verify our result.

3.4.2. CME Detection

The AR produces an eruption after the formation of the sigmoid. As the eruption occurred on-disk, the projection effect reduces the contrast and consequently limits the visibility of the faint eruption on-disk in EUV/AIA intensity images. But upon applying the running difference technique to AIA 171 Å images, we can observe the propagation of the CME flux

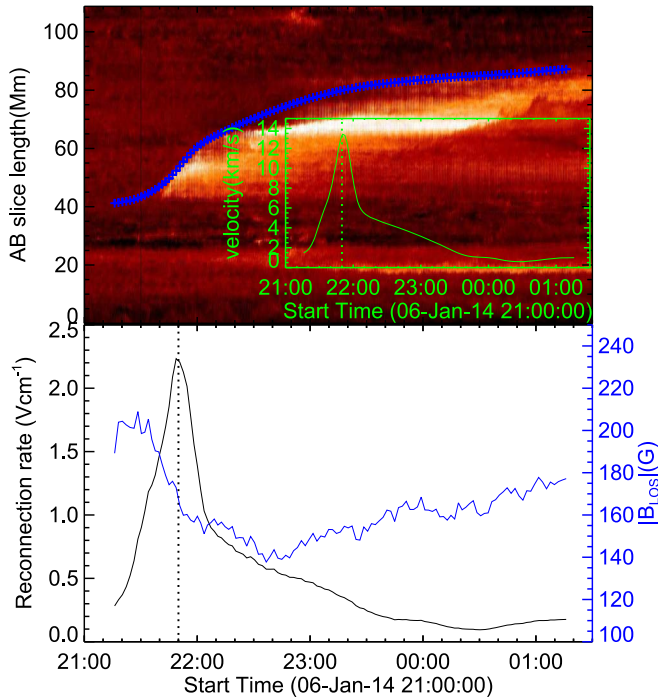


Figure 5. Top panel: spacetime plot of slice AB (Figure 3(c)) generated from AIA 304 Å images. The bright section traces the motion of the flare ribbon. The blue “+” symbols represent the spline fit to the distance data points and the inset (green) shows the temporal profile of the ribbon velocity derived from the time derivative of the spline-smoothed distance profile. Bottom panel: temporal evolution of local reconnection rate (black) and absolute mean LOS magnetic field strength (blue), swept by the flare ribbons. The velocity and reconnection rate profiles are temporally well correlated and both peak at 21:47 UT (vertical dotted line), corresponding to the flare peak time.

rope unambiguously. Figures 7(a)–(d) represent the sequential expansion and eruption of CME from the source AR in the northwest direction. To filter out high-frequency features and to improve contrast, we apply a high degree of smoothing to the 5 minute running difference images of AIA 171 Å. The traced gray line in panel 7(c) represents the stretching and expanding CME front, while still having connections to its source AR. Panel 7(d) represents the post-eruption scenario in which, as the CME moves away from the limb, the stretched loops shrink to form the cusp-shaped structure below. This eruption scenario matches with the catastrophic CME model. This leads to the stretching up of overlying loops and as a result opposite field loop lines start getting close to each other in a cusp-shaped structure. As the loops came into contact with each other, the current sheet formed between them and the subsequent reconnection in the current sheet led to formation of the post-CME loops below. Panels 7(e)–(f) display the observed CME in the LASCO C2 and C3 fields of view (FOV), respectively.

3.4.3. CME Kinematics

We performed on-disk kinematic analysis of the CME using 5 minute running difference images of AIA 171 Å. Upon careful inspection of running difference images, we identified the leading edge of the CME flux rope and placed a slit along its ascending direction. Since the eruption occurred on-disk, the height refers to the projected distance on the disk from the center of the Sun. Thus, the resulting on-disk velocity of the CME flux rope is also approximated. The spacetime image is shown in the top panel of Figure 8 and the blue “+” symbols in

the image represent an ascending CME front. We used a model containing the linear term to treat the slow-rise phase and an exponential term to account for the rapid-acceleration phase as described in Cheng et al. (2013) and is given by $h(t) = C_0 e^{(t-t_0)/\tau} + C_1(t-t_0) + C_2$, where $h(t)$ is height at a given time t , and τ , t_0 , C_0 , C_1 , and C_2 are free coefficients. This model has two distinct advantages: (1) a single function describes the two phases of eruption effectively and (2) it provides a convenient method to determine the time of the onset of the rapid-acceleration phase (T_c). The onset of the rapid-acceleration phase is defined as the time at which the exponential component of velocity equals its linear component as $T_c = \tau \ln(C_1\tau/C_0) + t_0$. We used `mpfit.pro` to fit the height–time data. From the fit, T_c is determined to be 21:51 UT (indicated by the vertical dashed line in the bottom panel of Figure 8).

Furthermore, the numerical derivative method is applied to calculate the velocity and acceleration profiles (e.g., Zhang et al. 2001, 2004). The derived velocity (blue) and acceleration (red) profiles are overplotted in the bottom panel of Figure 8. The duration of the slow-rise phase is between 21:32 and 21:51 UT, with an average velocity of 26 km s^{-1} . By 21:51 UT, the CME front acquired fast-rise motion and velocity (acceleration) increased from 36 km s^{-1} (14 m s^{-2}) to 206 km s^{-1} (134 m s^{-2}) in 54 minutes, with an average acceleration of $\approx 55 \text{ m s}^{-2}$. These are quite different from the strong eruption cases; for example, Zhang et al. (2012) showed that the CME flux rope in the slow-rise phase has an average velocity of about 60 km s^{-1} and in the fast-rise phase it reached a terminal velocity of about 700 km s^{-1} in 6 minutes, with an average acceleration of 1600 m s^{-2} . In another example of a moderately strong eruption event, presented in Cheng et al. (2014), the CME flux rope had an average velocity of about 35 km s^{-1} during its slow-rise phase and in the rapid-acceleration phase it reached a terminal velocity of about 300 km s^{-1} in 23 minutes, with an average acceleration of 200 m s^{-2} . Thus, the eruption under study is a much slower one and we opine that the slow-rise phase of the CME flux rope is due to the tether-cutting reconnection, and the fast-rise phase is accounted for by the catastrophic behavior of the flux rope system and/or torus instability (Démoulin & Aulanier 2010; Chen et al. 2018). This will be discussed further in Section 4.

The sigmoid eruption is observed as CME by *SOHO*/LASCO and cataloged as two separate CMEs appearing in the LASCO C2 FOV initially at 23:12 UT and 23:24 UT at position angles 275° and 300° , respectively. We believe that these could be different parts of a single CME structure, and refer to them as part 1 and part 2. Part 1 was identified as an expanding CME front, as observed in AIA 171 Å difference images of Figures 7(a)–(d) (also refer to the online animated figure). Furthermore, it was tracked by coronagraph C3 until January 7 at 00:42 UT up to a height of $9 R_\odot$. Part 2 was tracked by coronagraph C3 until January 7 at 8:00 UT up to a height of $22 R_\odot$. The height–time plot available in the *SOHO*/LASCO CME catalog shows the linear speeds of part 1 and part 2 as 722 km s^{-1} and 442 km s^{-1} , with angular widths of 15° and 100° , respectively. Gopalswamy et al. (2001) found that the average speed of CMEs associated with decameter–hectometric radio type II bursts is 960 km s^{-1} and the average width is 66° . In other words, the strong geo-effective CMEs are those with speeds and width greater than 960 km s^{-1} and 66° , respectively. Therefore, the CME event under study is considered a slow/weak CME.

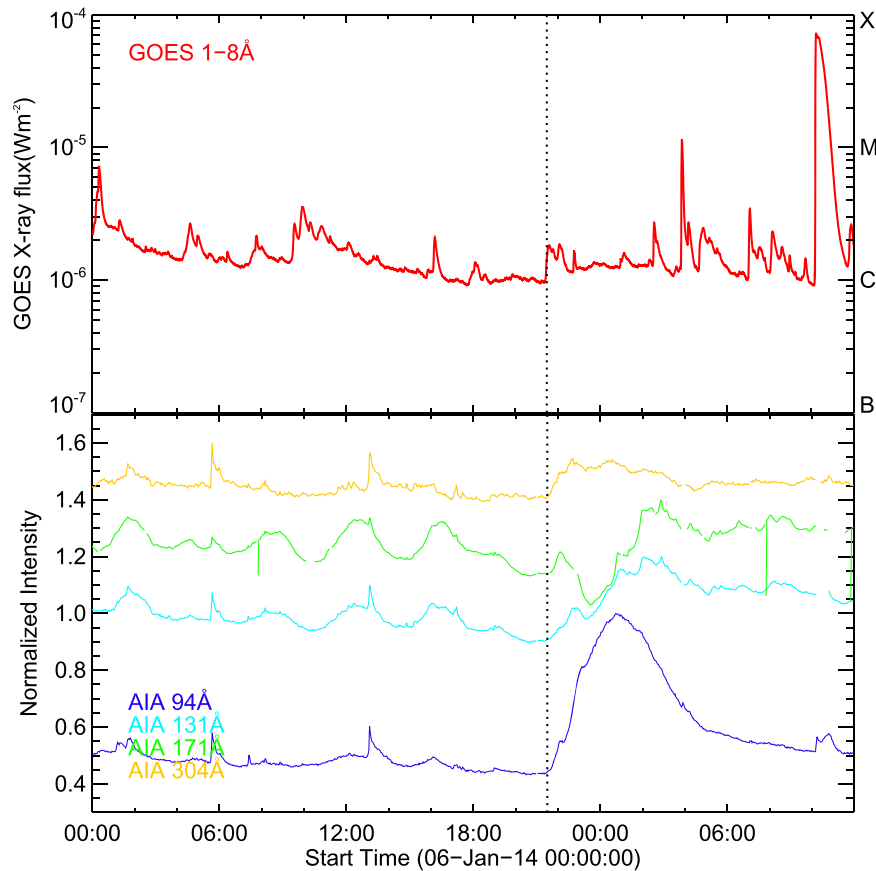


Figure 6. Top panel: temporal evolution of disk-integrated *GOES* SXR flux in 1–8 Å. Bottom panel: light curves of AR 11942 in EUV wavebands of AIA. The vertical dotted line marks the onset time (21:32 UT) of the main-phase reconnection. Vertical shifts (relative) to each light curve were given for better presentation. Note that the AIA 304 Å and 94 Å light curves start increasing with the onset of reconnection at 21:32 UT on January 6 and peak at 22:40 UT on January 6, 00:44 UT on January 7, respectively.

3.4.4. Relaxation of Sheared Core Field

Past observations (Sterling et al. 2000; Pevtsov 2002; Liu et al. 2010) have shown that eruptive ARs, which initially display a sigmoidal structure, evolve into a post-eruption phase that consists of field lines with a cusp-like shape. The newly formed field lines of sigmoidal structure are highly sheared, containing much non-potential magnetic energy. The reconnection that occurs in a sheared core field (Moore et al. 2001) helps with the release of such contained free magnetic energy. The dissipation of free magnetic energy causes the sheared field to relax, giving rise to the contraction of loops (Ji et al. 2007). This process of relaxation of sheared field lines is represented by typical AIA 94 Å passband images. By 01:00 UT, the CME moved away from the sheared core field, and the enhanced brightness in the core field indicates the continuous reconnections allowing the long sheared field lines to relax, as seen in EUV observations (figure not shown).

3.5. Thermal Evolution

The emission measure and thermal structure of sigmoids are explored by applying differential emission measure (DEM) analysis to six EUV passbands of *SDO/AIA*. We used `xrt_dem_iterative2.pro` in Solar Software with modifications to work with AIA data. The code was initially designed for *Hinode/X-ray Telescope* data (Golub et al. 2004; Weber et al. 2004). However, Cheng et al. (2012) tested this

code extensively on AIA data by studying the different thermal properties of multi-structure CME. The DEM maps of sigmoid are constructed and the emission measure (EM) and DEM weighted average temperature (\bar{T}) are derived using the following definitions:

$$\bar{T} = \int \text{DEM}(T)T dt / \int \text{DEM}(T) dt; \quad \text{EM} = \int \text{DEM}(T) dt, \quad (1)$$

where integration is performed with temperature limits of $5.7 < \text{Log } T < 7.1$. In Figure 9, we plot the maps of EM and \bar{T} representing the distribution of total emission measure and the average temperature of sigmoidal structure in the middle and bottom panels, respectively, while the corresponding AIA 131 Å images are displayed in the top panel. The distribution of EM and \bar{T} in sigmoidal structure is higher than that of the quiet region surrounding it in all panels. As the magnetic reconnection had already started at 21:32 UT, the enhanced brightness is clearly seen in the AIA 131 Å image taken at 22:00 UT at the reconnection site. Similarly, in the same time slab, the enhanced EM and \bar{T} distribution is seen in the reconnection region. The released energy due to magnetic reconnection heats up the plasma, resulting in the emission. At 23:00 UT, the hot post-eruption loops form below, resulting in an increase of the temperature and EM in and around those loop

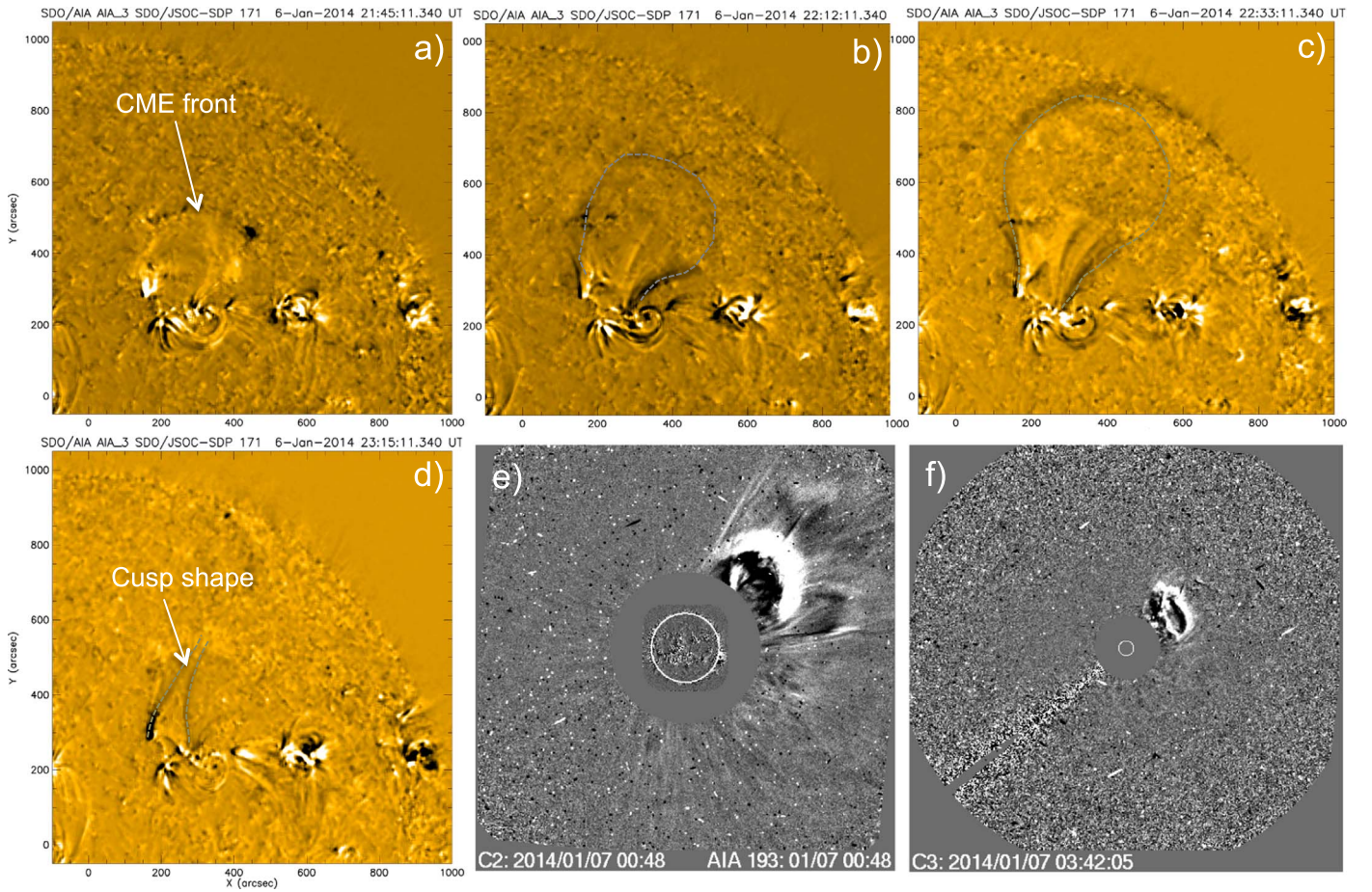


Figure 7. Image sequence of CME flux rope eruption from AR 11942. (a)–(d): time difference images of AIA 171 Å observations. To enhance the CME front, the actual observations are smoothed before taking the time difference. A cusp-shaped loop structure is visible below, leaving the CME blob that is shown in panel (d). (e)–(f): further propagation of the CME in LASCO C2 and C3. The AIA 171 Å image sequence runs from 21:03 UT on 2014 January 6 to 23:36 UT on 2014 January 6 (this is the first 4 s of the animation); the LASCO images run from 23:36 UT on 2014 January 6 to 04:30 UT on 07 Jan 2014 (this is the remaining 3 s of the animation).

(An animation of this figure is available.)

lines. At 00:15 UT on January 7, the EM and \bar{T} distribution reaches a maximum in and/or around bright reconnected loops. The EM reaches a maximum value of 10^{29} cm^{-5} and the average temperature (\bar{T}) reaches up to $10^{7.09}$ K. However, the maps are scaled optimally for better contrast. After 1:00 UT, the decrease in the EM and \bar{T} distribution starts, as shown by the time slab at 3:00 UT.

The DEM reconstruction is an ill-posed problem and several errors arise from uncertainties in the response function: background determination, radiative transfer effects, etc., (Judge 2010). Hence, we concentrated on the temporal variation of EM and \bar{T} rather than their exact values. We estimated the average values of EM and \bar{T} of the sigmoidal structure with the same FOV, as shown in Figure 9 during the time period from 21:30 UT to 04:00 UT at an interval of 15 minutes. The temporal evolutions of these curves are shown in Figure 10. As the CME moves away from the solar disk (by 22:50 UT), the hot post-eruption loops form underneath. Due to this, the temperature and EM curves start to rise after the eruption. The EM curve in black and the \bar{T} curve in blue both follow the same trend, reaching their peaks at 00:15 UT, as indicated by the vertical dashed line in Figure 10. After reaching their peak, the average \bar{T} curve shows the gradual

declining phase, whereas the EM curve shows the steady phase until 02:00 UT and then declines. This shows that the emission from cooling loops is strong enough and comparable to that of hotter loop structures during that time period. Also, these curves follow the light curves of sigmoid as described in Section 3.4.1.

3.6. Evolution of Photospheric Magnetic Parameters

We studied the temporal evolution of different magnetic measures for 3 days (2.4 days prior to eruption) using the HMI vector magnetograms (SHARP series) at a cadence of 12 minutes. Generally, the magnetogram measures are area-dependent, hence these parameters are computed by choosing an area within the AR including an eruption region with a minimum flux-imbalance (i.e., net flux/total unsigned flux < 3%). Moreover, a careful manual inspection of field-line connectivity in AIA 171 Å images results in the exclusion of certain regions of AR connecting to neighboring ARs and thereby restricting the area only to the eruption region with minimum field lines connecting outside of it. The area enclosed by the white dashed rectangle in Figure 11(e) is used to compute the following magnetogram measures.

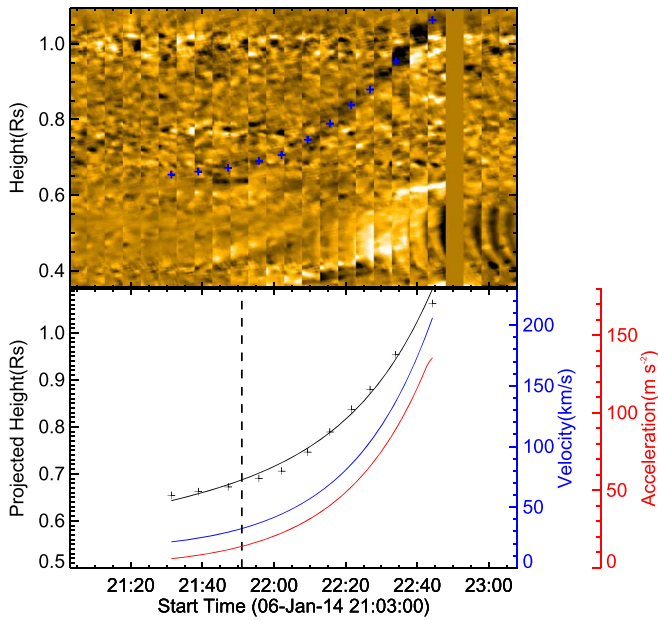


Figure 8. Top panel: spacetime stack plot of the slit placed across the expanding CME front observed in AIA 171 Å difference images. Bottom panel: projected height–time plot of the expanding CME front. “+” symbols (in both panels) trace the ascending CME front. The black solid curve is a model fit to the height–time data, and the blue (red) curve is the derived velocity (acceleration) of the CME front. The vertical dashed line (21:51 UT) represents the onset of the rapid-acceleration phase and it divides the eruption that occurred into two phases: the slow-rise phase lasting 21:32–21:51 UT, with an average velocity of 26 km s^{-1} , and the rapid-acceleration phase from 14 m s^{-2} to 134 m s^{-2} that lasted 54 minutes.

The total unsigned flux of an AR is defined as $\Phi = \sum |B_z| dA$, where dA is the area of an observation pixel. The flux is computed from the pixels with magnetic field strength higher than 50 G. Since the measurement error is within 15 G, we have chosen a threshold three times larger than that, hence the error in our estimation of flux is negligible. The temporal evolution of net flux is shown in Figure 11(a). The frequent emergence and cancellation of fluxes are evident in the AR during its disk passage from January 4 to January 7. Notable observations are from 4:00 UT on January 6 (as indicated by the vertical dashed line in Figure 11), where the net flux starts decreasing, corresponding to flux cancellation, and that decrease continues until the onset (21:32 UT; indicated by the vertical gray line in Figure 11) of the main-phase reconnection. During this time period, the filament exhibits dynamical evolution and rise motion, beginning at 05:35 UT. The regions of flux cancellation during this time period are studied in Section 3.2. Careful scrutiny of simultaneous observations of magnetograms and AIA images (we observed several episodes of EUV brightenings and also converging motions in small regions) led to the selection of two sub-regions, namely SR1 and SR2, as indicated in Figures 11(e)–(g). The net flux in these regions is plotted in the bottom panels, which show continuous decreasing evolution. We thus suggest from this observational evidence that the persistent slow shearing and converging motions about the PIL played a prime role in the cancellation of fluxes, leading to the initiation and eruption of the sigmoid configuration (Green & Kliem 2009; Green et al. 2011; Savcheva et al. 2012; Vemareddy & Mishra 2015; Vemareddy 2017b).

The vertical current density is computed as $J_z = 1/\mu_0 (\partial B_y/\partial x - \partial B_x/\partial y)$, where B_x and B_y represent the horizontal

component of the magnetic field. For a given polarity, the current distribution contains both positive and negative values. We examined the degree of net current neutralization (NCN) in each polarity by obtaining the ratio of direct current (DC) and return current (RC) (Török et al. 2014). The dominance of the signed currents decides the chirality of the magnetic field, so DC is also considered the dominant current and RC is the non-dominant current. The DC and RC are computed for each polarity by integrating current density values of different signs separately. This has been done only for those pixels with B_x , B_y values larger than 150 G and B_z values larger than 50 G to minimize the error in the computation of currents. The ratio of DC and RC indicates the extent of departure from net current neutralization in any polarity. While selecting the integration area, we have not excluded the non-eruptive flux completely in the AR, so the values of $|\text{DC}/\text{RC}|$ of any polarity at any time interval are expected to be smaller than the actual values, which are estimated by restricting the integration to the foot point area of eruptions (Liu et al. 2017; Vemareddy 2017a). We found that DC is positive in the south polarity and negative in the north polarity. The temporal evolutions of $|\text{DC}/\text{RC}|$ values in both polarity regions are plotted in Figure 11(b). The $|\text{DC}/\text{RC}|$ values in the south polarity region are maintained well above unity. Although the evolution in north polarity has a similar trend, the $|\text{DC}/\text{RC}|$ values fluctuate because the horizontal field in this polarity is not strong and the numerical differentiation may have artifacts to represent reliable current distribution. The non-neutralization current describes the eruptive behavior of AR in terms of flux rope models.

Average alpha (α_{av}), the proxy representing the twist of magnetic field lines in an AR, is computed using the equation given by $\alpha_{\text{av}} = \sum [J_z(x, y) B_z(x, y) / |B_z(x, y)|]$ (Pevtsov et al. 1994; Hagino & Sakurai 2004). The errors are estimated from the least-squared regression plot of B_z and J_z (Vemareddy et al. 2012). The temporal evolution of α_{av} and its error bars are shown in Figure 11(c). The twist of field lines increases from January 4 until January 6, consistent with coronal observations of sigmoidal structure formation over a timescale of days as described in Figure 1. As soon as the flux cancellation starts, i.e., at 4:00 UT on January 6, α_{av} decreases as the signature of disappearing flux from cancellation.

Furthermore, the total magnetic energy and potential energy in the coronal field are estimated using a Virial theorem equation (Chandrasekhar 1961; Molodensky 1974; Low 1982): as $E = \frac{1}{4\pi} \int (xB_x + yB_y) B_z dx dy$. Since the photospheric field is not force-free, the energy estimate from using this equation serves as a proxy for the energy content in the AR. Then, the proxy for magnetic free energy is estimated by taking the difference between the total magnetic energy and potential energy. We used the whole AR for potential-field extrapolation but energy estimations were done for the region within the white dashed rectangle as shown in Figure 11(e). As seen in panel 11(d), the free energy decreases, corresponding to the increasing α_{av} until January 6. This may be due to the emerging flux, which increases the potential energy more than it increases the non-potential amount of the total energy. During the magnetic flux cancellation period (4:00 UT–21:32 UT, 6 January), the free energy remains almost the same, with some undulations. It is important to note that the free energy during the small C-class flare event is small and the field variations at different sub-regions camouflage the field contributing to the reconnecting flux. In such cases the expected variation of the

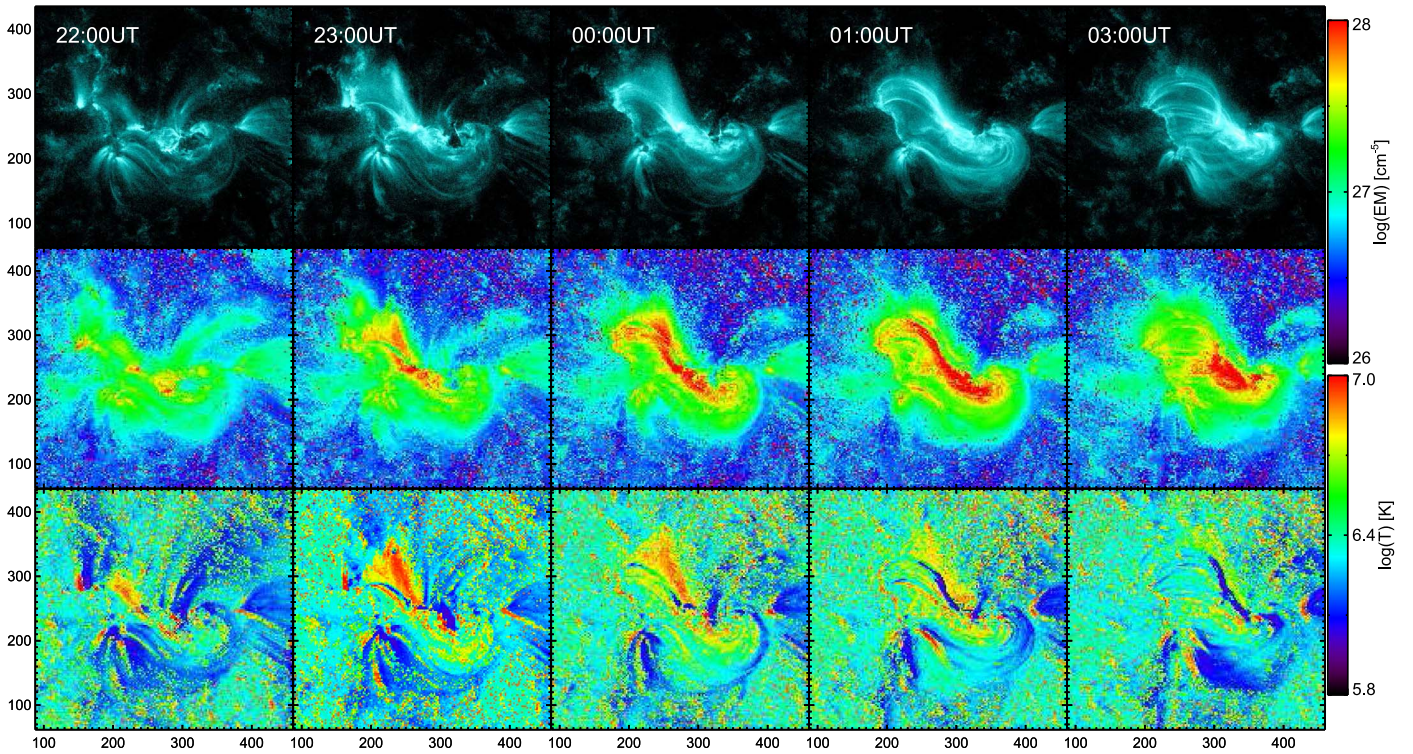


Figure 9. Top row: AIA 131 Å waveband images representing the typical evolution of a sigmoid. Middle row: maps of EM distribution corresponding to the panels in the first row. Bottom row: maps of T distribution. In the third and fourth columns, the EM and T distribution reaches its maximum in and/or around bright reconnected loops.

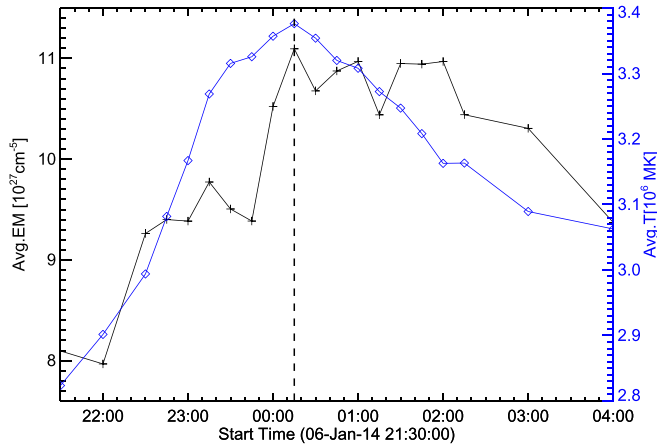


Figure 10. Temporal evolution of average EM and \bar{T} in the AR. The dashed vertical line represents the peak time (00:15 UT) of both curves. The \bar{T} curve gradually declines from its peak but the EM profile shows steady emission until 2:00 UT, indicating strong emissions from cooling loops and then a slow decline.

free energy is difficult to realize, in addition to the intrinsic problems with noisy transverse field observations. In conclusion, this study suggests that the energy release proceeded over a much longer duration of time, manifesting in a filament rise and an eventual eruption driven by converging and canceling flux in the photosphere.

4. Summary and Discussion

In this paper, we investigated the sigmoidal eruption from AR 11942 on 2014 January 6 that led to a CME accompanied by a weak flare. We presented a comprehensive study of

morphological transformation from a simple bipolar configuration to a complicated inverse sigmoidal AR, along with its initiation and eruption mechanisms, using the multi-wavelength EUV observations from AIA and (vector) magnetograms from HMI. The flare and CME are detected by flare ribbon evolution and running difference images, respectively.

Initially, the AR is compact and bipolar in nature, and evolved to a sheared configuration consisting of inverse J loops over a couple of days (Figure 1). Magnetic flux dispersion, shearing and converging motion are observed to play a significant role in the development of the sigmoidal structure hosting a filament channel, as inferred from EUV observations of AIA. Such evolution leads to flux cancellation and net flux decrease starts early on January 6. Consequently, the filament channel initiated upward motion from 5:35 UT on January 6. As a result, tether-cutting reconnection of inverse J-loops leads to the formation of continuous inverse S-shaped loops as a flux rope (Moore et al. 2001; Amari et al. 2003). While tether-cutting reconnection continues under the converging and shearing motions, the sigmoidal structure loses equilibrium at 21:32 UT, leading to a CME and weak flare. Forbes & Isenberg (1991) indicated that as flux cancellation continues near the magnetic neutral line, the flux rope embedded in a bipolar field rises smoothly until it reaches a critical point, at which the flux rope demonstrates a catastrophic behavior, i.e., after the gradual accumulation of magnetic energy, the flux-rope system transits from a stable state to an unstable one containing a current sheet. The catastrophe model of solar eruptions suggests the catastrophic loss of mechanical equilibrium in the magnetic configuration (e.g., Forbes 2000; Priest & Forbes 2002; Lin 2004).

Figure 7(c) shows that when the flux rope rises, the overlying loops get stretched and the inward motion of

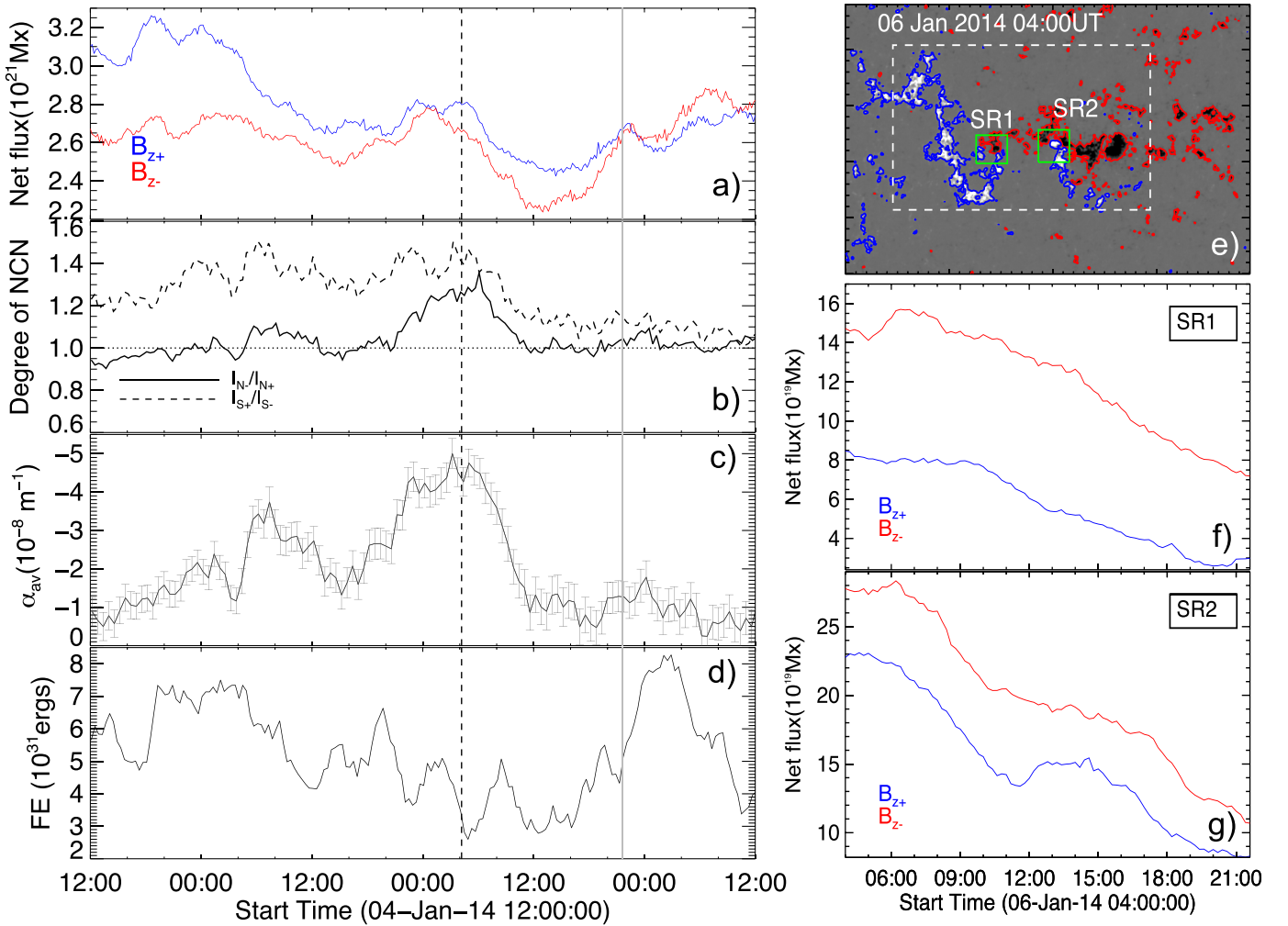


Figure 11. Time evolution of magnetic parameters in the region enclosed by a white dashed rectangle in panel (e). (a): Net flux; (b): degree of net current neutralization; (c): α_{av} ; (d): free magnetic energy at the photosphere. The vertical dashed line (04:00 UT) marks the time when net flux starts decreasing until the time of eruption (21:32 UT), which is indicated by the vertical gray line. Also, note that the currents are non-neutralized before and during the time of eruption. (e)–(g) Net flux evolution in converging sub-regions SR1 and SR2. Note that the net flux in the sub-regions shows decreasing flux content over time.

anti-parallel magnetic field lines leads to the formation of a thin current sheet, where the magnetic reconnection sends large amount of the reconnected flux and plasma outward, accounting for the rapid expansion of the ejecta (plasma blobs or plasmoids or CME) and the hot shell surrounding it (Lin 2004). Here, the smoothness of the observed eruption is accounted for by the slow reconnection process (local reconnection rate range $0.01\text{--}2.14\text{ V cm}^{-1}$) in the current sheet underneath the flux rope. Depending on the amount of reconnected flux, the magnitude of flare emission is visible in X-rays. The smaller the hoop/self force in the flux rope, the smaller the coronal disturbance, and the slower is the CME and its impact. We believe that a small number of inverse J-shaped loops participated in the tether-cutting reconnection, resulting in the weak flux rope and the rest of the sheared arcade being relaxed after the eruption. This is clear from the canceling/converging small flux regions with weak PIL. Accordingly, a mild SXR enhancement is observed due to a slow reconnection rate followed by a dominant EUV emission in the late phase of eruption. So, studying such weak events is important for learning the connection between photospheric evolution and the origin of eruptions that affect the Earth.

Démoulin & Aulanier (2010) and Kliem et al. (2014) showed that the critical conditions for the catastrophic loss of equilibrium also satisfy the torus instability criterion. The rapid decaying of overlying magnetic field with height is referred to as torus instability and is measured with decay index $n(z) = -\frac{z}{B_h} \frac{\partial B_h}{\partial z}$, where z is the geometrical height from the bottom boundary and B_h is the horizontal field strength. We computed the background field for the entire volume of AR with potential magnetic field approximation. In Figure 12, the $n(z)$ is plotted as a solid curve and B_h is plotted as a dashed line. A constant value of $n_{crit} = 1.5$ is assumed as critical decay index, which corresponds to a critical height of 41.5 Mm. This agrees with past studies (Cheng et al. 2011; Vemareddy & Zhang 2014; Vasantharaju et al. 2018) in which the critical heights of eruptive events fall below 42 Mm.

The magnetic non-potential parameters α_{av} , NCN, show increasing behavior with the formation of the sigmoid by slow flux motions for two days prior to the eruption. However, the eruption occurs in a flux cancellation scenario by converging motions from 04:00 UT on January 4. During this period, the free energy exhibits almost steady behavior and α_{av} has a decreasing profile, contrary to the cases of stronger eruptions

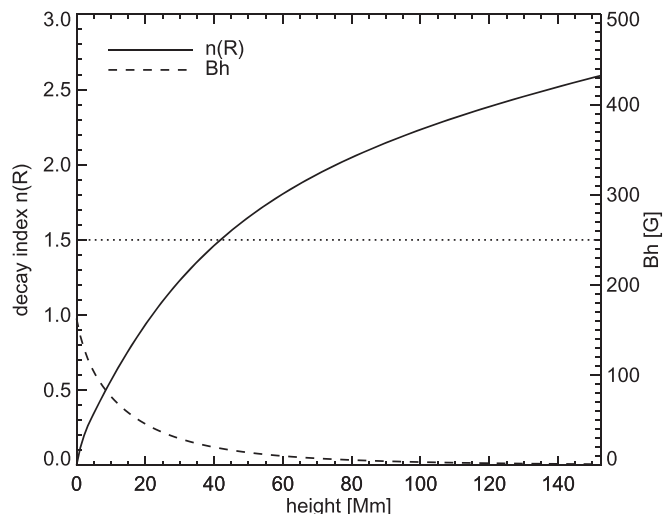


Figure 12. Decay index $n(z)$ with respect to height. The horizontal magnetic field strength, B_h (dashed curve), is plotted on the y-axis. The horizontal dotted line represents the critical decay index.

(Gibb et al. 2014; Vemareddy & Zhang 2014). It may be the case that the energy release is proceeded by a much longer time duration, manifesting the onset of the filament rise and eventual eruption driven by converging and canceling flux in the photosphere.

The eruptions from large ARs are usually associated with one or more clearly visible flux ropes in hot AIA channels. These are associated with sigmoids and filaments/prominences, and erupt as CMEs with strong X-ray flares (Vemareddy & Zhang 2014; Vemareddy 2017b; Dhakal et al. 2018). In contrast, the presented case is from an AR where converging/canceling flux region is small, with a weak PIL ensuing from a slow reconnection; yet it was still able to produce a successful eruption.

SDO is a mission of NASA's Living With a Star Program. N.V, a CSIR-SRF, gratefully acknowledges the funding from CSIR-HRDG, New Delhi. P.V. is supported by an INSPIRE grant of AORC scheme under the Department of Science and Technology. We thank the referee for the many detailed comments and suggestions.

ORCID iDs

N. Vasantharaju <https://orcid.org/0000-0003-2336-5208>

P. Vemareddy <https://orcid.org/0000-0003-4433-8823>

References

Amari, T., Luciani, J. F., Aly, J. J., Mikic, Z., & Linker, J. 2003, *ApJ*, **585**, 1073

Antiochos, S. K., DeVore, C. R., & Klimchuk, J. A. 1999, *ApJ*, **510**, 485

Aulanier, G., Török, T., Démoulin, P., & DeLuca, E. E. 2010, *ApJ*, **708**, 314

Bemporad, A., Poletto, G., Suess, S. T., et al. 2006, *ApJ*, **638**, 1110

Bobra, M. G., Sun, X., Hoeksema, J. T., et al. 2014, *SoPh*, **289**, 3549

Brueckner, G. E., Howard, R. A., Koomen, M. J., et al. 1995, *SoPh*, **162**, 357

Canfield, R. C., Hudson, H. S., & McKenzie, D. E. 1999, *GeoRL*, **26**, 627

Carmichael, H. 1964, *NASSP*, **50**, 451

Chae, J., Moon, Y.-J., & Pevtsov, A. A. 2004, *ApJL*, **602**, L65

Chamberlin, P. C., Milligan, R. O., & Woods, T. N. 2012, *SoPh*, **279**, 23

Chandrasekhar, S. 1961, *Hydrodynamic and Hydromagnetic Stability* (Oxford: Clarendon)

Chen, H., Duan, Y., Yang, J., Yang, B., & Dai, J. 2018, *ApJ*, **869**, 78

Chen, P. F. 2011, *LRSF*, **8**, 1

Chen, Y., Hu, Y. Q., & Xia, L. D. 2007, *AdSpR*, **40**, 1780

Cheng, X., Ding, M. D., Guo, Y., et al. 2014, *ApJ*, **780**, 28

Cheng, X., Zhang, J., Ding, M. D., et al. 2013, *ApJL*, **769**, L25

Cheng, X., Zhang, J., Ding, M. D., Guo, Y., & Su, J. T. 2011, *ApJ*, **732**, 87

Cheng, X., Zhang, J., Saar, S. H., & Ding, M. D. 2012, *ApJ*, **761**, 62

Dai, Y., Ding, M., Zong, W., & Yang, K. E. 2018, *ApJ*, **863**, 124

Démoulin, P., & Aulanier, G. 2010, *ApJ*, **718**, 1388

Dhakal, S. K., Chintzoglou, G., & Zhang, J. 2018, *ApJ*, **860**, 35

Falconer, D. A. 2001, *JGR*, **106**, 25185

Falconer, D. A., Moore, R. L., & Gary, G. A. 2003, *JGRA*, **108**, 1380

Forbes, T. G. 2000, *JGR*, **105**, 23153

Forbes, T. G., & Isenberg, P. A. 1991, *ApJ*, **373**, 294

Forbes, T. G., & Lin, J. 2000, *JASTP*, **62**, 1499

Forbes, T. G., & Priest, E. R. 1984, in *Solar Terrestrial Physics: Present and Future*, NASA RP-1120, ed. D. M. Butler & K. N. Papadopoulos (Washington, DC: NASA), 1

Gibb, G. P. S., Mackay, D. H., Green, L. M., & Meyer, K. A. 2014, *ApJ*, **782**, 71

Gibson, S. E., Fan, Y., Török, T., & Kliem, B. 2006, *SSRv*, **124**, 131

Golub, L., DeLuca, E. E., Sette, A., & Weber, M. 2004, in *ASP Conf. Ser. 325, The Solar-B Mission and the Forefront of Solar Physics*, ed. T. Sakurai & T. Sekii (San Francisco, CA: ASP), 217

Gopalswamy, N., Yashiro, S., Kaiser, M. L., Howard, R. A., & Bougeret, J.-L. 2001, *JGR*, **106**, 29219

Green, L. M., & Kliem, B. 2009, *ApJL*, **700**, L83

Green, L. M., Kliem, B., & Wallace, A. J. 2011, *A&A*, **526**, A2

Hagino, M., & Sakurai, T. 2004, *PASJ*, **56**, 831

Hinterreiter, J., Veronig, A. M., Thalmann, J. K., Tschernitz, J., & Pötzi, W. 2018, *SoPh*, **293**, 38

Hirayama, T. 1974, *SoPh*, **34**, 323

Hood, A. W., & Priest, E. R. 1979, *SoPh*, **64**, 303

Ji, H., Huang, G., & Wang, H. 2007, *ApJ*, **660**, 893

Judge, P. G. 2010, *ApJ*, **708**, 1238

Kliem, B., Lin, J., Forbes, T. G., Priest, E. R., & Török, T. 2014, *ApJ*, **789**, 46

Kliem, B., & Török, T. 2006, *PhRvL*, **96**, 255002

Kopp, R. A., & Pneuman, G. W. 1976, *SoPh*, **50**, 85

Leka, K. D., & Barnes, G. 2003a, *ApJ*, **595**, 1277

Leka, K. D., & Barnes, G. 2003b, *ApJ*, **595**, 1296

Lemen, J. R., Title, A. M., Akin, D. J., et al. 2012, *SoPh*, **275**, 17

Lin, J. 2004, *SoPh*, **219**, 169

Lin, J., & Forbes, T. G. 2000, *JGR*, **105**, 2375

Lin, J., Ko, Y.-K., Sui, L., et al. 2005, *ApJ*, **622**, 1251

Liu, K., Wang, Y., Zhang, J., et al. 2015, *ApJ*, **802**, 35

Liu, K., Zhang, J., Wang, Y., & Cheng, X. 2013, *ApJ*, **768**, 150

Liu, R., Liu, C., Wang, S., Deng, N., & Wang, H. 2010, *ApJL*, **725**, L84

Liu, Y., Sun, X., Török, T., Titov, V. S., & Leake, J. E. 2017, *ApJL*, **846**, L6

Low, B. C. 1982, *SoPh*, **77**, 43

Miklenic, C. H., Veronig, A. M., Vršnak, B., & Hanslmeier, A. 2007, *A&A*, **461**, 697

Molodensky, M. M. 1974, *SoPh*, **39**, 393

Moore, R. L., & Labonte, B. J. 1980, in *IAU Symp. 91, Solar and Interplanetary Dynamics*, ed. M. Dryer & E. Tandberg-Hanssen (Dordrecht: Reidel), 207

Moore, R. L., Sterling, A. C., Hudson, H. S., & Lemen, J. R. 2001, *ApJ*, **552**, 833

Pesnell, W. D., Thompson, B. J., & Chamberlin, P. C. 2012, *SoPh*, **275**, 3

Pevtsov, A. A. 2002, *SoPh*, **207**, 111

Pevtsov, A. A., Canfield, R. C., & Latushko, S. M. 2001, *ApJL*, **549**, L261

Pevtsov, A. A., Canfield, R. C., & Metcalf, T. R. 1994, *ApJL*, **425**, L117

Pevtsov, A. A., Canfield, R. C., & Metcalf, T. R. 1995, *ApJL*, **440**, L109

Priest, E. R., & Forbes, T. G. 2002, *A&ARv*, **10**, 313

Rust, D. M., Anderson, B. J., Andrews, M. D., et al. 2005, *ApJ*, **621**, 524

Rust, D. M., & Kumar, A. 1996, *ApJL*, **464**, L199

Savcheva, A. S., Green, L. M., van Ballegoijen, A. A., & DeLuca, E. E. 2012, *ApJ*, **759**, 105

Scherer, P. H., Schou, J., Bush, R. I., et al. 2012, *SoPh*, **275**, 207

Schrijver, C. J. 2007, *ApJL*, **655**, L117

Schuck, P. W. 2006, *ApJ*, **646**, 1358

Seehafer, N. 1990, *SoPh*, **125**, 219

Song, H. Q., Chen, Y., Ye, D. D., et al. 2013, *ApJ*, **773**, 129

Sterling, A. C., Hudson, H. S., Thompson, B. J., & Zarro, D. M. 2000, *ApJ*, **532**, 628

Sturrock, P. A. 1966, *Natur*, **211**, 695

Török, T., Kliem, B., & Titov, V. S. 2004, *A&A*, **413**, L27

Török, T., Leake, J. E., Titov, V. S., et al. 2014, *ApJL*, **782**, L10

van Ballegoijen, A. A., & Martens, P. C. H. 1989, *ApJ*, **343**, 971

- Vasantharaju, N., Vemareddy, P., Ravindra, B., & Doddamani, V. H. 2018, *ApJ*, 860, 58
- Vemareddy, P. 2017a, *ApJ*, 851, 3
- Vemareddy, P. 2017b, *ApJ*, 845, 59
- Vemareddy, P., Ambastha, A., & Maurya, R. A. 2012, *ApJ*, 761, 60
- Vemareddy, P., & Mishra, W. 2015, *ApJ*, 814, 59
- Vemareddy, P., & Zhang, J. 2014, *ApJ*, 797, 80
- Vourlidas, A., Lynch, B. J., Howard, R. A., & Li, Y. 2013, *SoPh*, 284, 179
- Weber, M. A., Deluca, E. E., Golub, L., & Sette, A. L. 2004, in IAU Symp. 223, Multi-Wavelength Investigations of Solar Activity, ed. A. V. Stepanov, E. E. Benevolenskaya, & A. G. Kosovichev (Cambridge: Cambridge Univ. Press), 321
- Zhang, J., Cheng, X., & Ding, M.-D. 2012, *NatCo*, 3, 747
- Zhang, J., Dere, K. P., Howard, R. A., Kundu, M. R., & White, S. M. 2001, *ApJ*, 559, 452
- Zhang, J., Dere, K. P., Howard, R. A., & Vourlidas, A. 2004, *ApJ*, 604, 420